



Full Text View

[Volume 29, Issue 8 \(August 1999\)](#)

Journal of Physical Oceanography

Article: pp. 1649–1665 | [Abstract](#) | [PDF \(644K\)](#)

Geometry of Cross-Stream Mixing in a Double-Gyre Ocean Model

A. C. Poje and G. Haller

Division of Applied Mathematics, Brown University, Providence, Rhode Island

(Manuscript received December 11, 1997, in final form July 14, 1998)

DOI: 10.1175/1520-0485(1999)029<1649:GOCSMI>2.0.CO;2

ABSTRACT

New dynamical systems techniques are used to analyze fluid particle paths in an eddy resolving, barotropic ocean model of the Gulf Stream. Specifically, the existence of *finite-time invariant manifolds* associated with transient, mesoscale events such as ring detachment and merger is proved based on computer-assisted analytic results. These “Lagrangian” invariant manifolds completely organize the dynamics and mark the pathways by which fluid parcels may be exchanged across stream. In this way, the Lagrangian flow geometry of a detaching ring or a ring–jet interaction event, as well as the exact associated particle flux, is obtained.

The detaching ring geometry indicates that a significant amount of the fluid entrained by the ring originates in a long thin region on the far side of the jet and that this region extends as far upstream as the western boundary current. In the ring–stream interaction case, particle transport occurs both to and from the ring and is concentrated in thin regions on the near side of the jet and around the perimeter of the ring.

1. Introduction

With the advent of long-lived, isopycnal floats, an extensive observational database of Lagrangian particle paths has become available for the Gulf Stream ([Bower and Rossby 1989](#); [Owens 1984](#)). The float data reveals a complicated, three-dimensional structure to the Lagrangian dynamics of the stream. Even in the upper layers where jet velocities and associated potential vorticity gradients are the highest, individual trajectories exhibit a large degree of fluctuation and incoherence. The observations of [Bower and Rossby \(1989\)](#) and [Song et al. \(1995\)](#) of the dataset indicate a considerable amount of exchange between the central jet and the surrounding fluid as evidenced by the large proportion of floats (72% in Song et al.) that are expelled from the stream in a relatively short period of time [$\sim O(1$ month)].

By coupling Lagrangian float data with available Eulerian satellite observations, Song et al., following previous work by [Bower and Rossby \(1989\)](#), identify three main mechanisms by which fluid particles are transferred from the stream to the surrounding fluid: ring generation, ring–stream interaction, and meandering. Of these, the meandering mechanism has received the most modeling attention. [Bower \(1991\)](#) postulated a kinematic model for a jet meandering with constant phase speed to describe the observed Lagrangian dynamics in the context of a simple Eulerian flow field. By adding periodic time

Table of Contents:

- [Introduction](#)
- [Finite time transport](#)
- [Numerical model](#)
- [Ring detachment](#)
- [Ring–stream interaction](#)
- [Discussion](#)
- [REFERENCES](#)
- [TABLES](#)
- [FIGURES](#)

Options:

- [Create Reference](#)
- [Email this Article](#)
- [Add to MyArchive](#)
- [Search AMS Glossary](#)

Search CrossRef for:

- [Articles Citing This Article](#)

Search Google Scholar for:

- [A. C. Poje](#)
- [G. Haller](#)

dependence to the meander speed, [Samelson \(1991\)](#) arrived at a system that displays “chaotic” advection; the mixing of fluid particles can be analyzed in terms of the geometry of intersecting stable and unstable manifolds and *lobe dynamics* (see, e.g., [MacKay et al. 1984](#); [Rom-Kedar et al. 1990](#); [Wiggins 1992](#)). More recently, such dynamical systems approaches have been extended to nearly time periodic, numerically generated vector fields such as tidally forced flow in the Gulf of Maine ([Ridderinkhof and Loder 1994](#)) and a dynamically consistent, quasigeostrophic model of a barotropic jet ([Lozier et al. 1997](#); [Miller et al. 1997](#)). The result is a systematic means of quantifying the Lagrangian transport between qualitatively different flow regimes.

While these studies provide strong support to the belief that chaotic advection plays a major role in transporting fluid parcels into and out of the stream, they concentrate on the nearly time periodic meandering mechanism. Here we wish to investigate the Lagrangian dynamics inherent in transient mixing events such as the formation and detachment of cold (warm) core rings and the interaction of already existent rings with the stream; the other two transport mechanisms in the nomenclature of Song et al.

Much of the previous work has been based on transport ideas born out of lobe dynamics, which requires restrictions on the flow studied. First, lobe dynamics requires the *infinite-time* existence of an organizing *hyperbolic* particle path that behaves like a saddle: it attracts particles exponentially from a certain set (its *stable manifold*) while it repels fluid particles from another set (its *unstable manifold*). In contrast, the available experimental or numerical data is clearly finite in time, but even within that finite time the existence of hyperbolic behavior is usually of transient nature in. Second, the stable and unstable manifolds of a hyperbolic trajectory are assumed to intersect in infinitely many *lobes*. While this condition generically holds for velocity fields with periodic or quasiperiodic time dependence, a typical aperiodic flow field will admit only finitely many lobes, or very often, none. Third, one has to know the location of invariant manifolds, that is, Lagrangian structures, in the flow field to carry out a transport study, while real-life flows are typically defined through an experimentally or numerically generated velocity field, that is, *Eulerian data*. Such a database only yields Lagrangian structures after numerical integration, which introduces further errors to the study of a problem that is only approximately defined to begin with.

This paper takes a different approach and targets the available Eulerian data directly in order to uncover the geometry of Lagrangian mixing due to intermittent, mesoscale events such as ring detachment, merger, and ring–jet interaction. We seek to answer the following questions: 1) How can one rigorously infer the existence of intense, local Lagrangian mixing from the numerical double gyre ocean model? 2) What is the set of fluid particles in the stream that gets entrained into a detaching ring, and conversely, which ring particles are reabsorbed into the stream during an interaction event? 3) How can one obtain computer-assisted analytic estimates for the life span of cross-gyre mixing and the associated flux from purely Eulerian observations without numerically integrating the velocity field?

To answer the above questions, we use recent results from dynamical systems theory given in [Haller and Poje \(1998\)](#). This theory assumes nothing special about the time dependence of the flow, focusing instead on the transport associated with the presence of *transient stagnation points* in the velocity field. Under a set of explicit (Eulerian) conditions, such stagnation points induce finite-time hyperbolicity in Lagrangian particle motions. The hyperbolicity is manifested by the existence of finite-time analogs of stable and unstable manifolds that, in turn, identify the exact location of particles that, for example, are eventually entrained by a detaching ring. Once the manifold geometry is known, analytic flux calculations and error estimates allow one to quantify the associated mixing between the jet and the ring. The idea of Lagrangian dynamics organized by moving or transient, “stagnation” points in the Eulerian frame has been used previously in connection with the evolution and filamentation of quasigeostrophic vortices (e.g., [Polvani et al. 1989](#); [Melander et al. 1987](#)). In the case of jet–eddy interactions, [Bell and Pratt \(1992\)](#) clearly state that a stagnation point must exist for “a significant percentage of an eddy turnover time” if the eddy is to strip fluid from the jet. The theoretical considerations in [section 2](#) of the present work allow one to explicitly estimate this existence time in terms of the Eulerian data.

In each mixing scenario, the calculation of finite-time invariant manifolds provides a considerable computational and conceptual simplification of the Lagrangian dynamics: One need only follow short *one-dimensional* segments of initial conditions (i.e., segments of the finite-time invariant manifolds) in order to obtain qualitative and quantitative information on a whole *two-dimensional* domain of interest. The locations of these structures at a given time unambiguously distinguish the regions of fluid that take part in the transport from those that do not.

While the analytic part of this work is the first application of finite-time mixing theory to a large numerical dataset, the numerical component of our study makes use of the tools developed by [Ridderinkhof and Loder \(1994\)](#), [Lozier et al. \(1997\)](#), and [Miller et al. \(1997\)](#) for the analysis of numerically generated vector fields.


A brief synopsis of the relevant background is presented in [section 2](#), where we sketch the mathematical aspects of finite-time mixing. The numerical model and general Eulerian setting are described in [section 3](#). In [section 4](#) we study the Lagrangian dynamics of particle entrainment into a detaching cold core ring, and similar analysis is conducted for the case of ring–stream interaction in [section 5](#). A summary of the results and discussion conclude the paper.

2. Finite time transport

In this section we describe the mathematical framework for transport in two-dimensional flows developed in [Haller and Poje \(1998\)](#). Here we only sketch the main results and refer the reader to that work for details.

We are concerned with incompressible velocity fields $\mathbf{u}(x, y, t) = (\mathbf{u}_1(x, y, t), \mathbf{u}_2(x, y, t))$ of the form

$$\begin{aligned} v_1 = \dot{x} &= \frac{\partial \psi(x, y, t)}{\partial y}, \\ v_2 = \dot{y} &= -\frac{\partial \psi(x, y, t)}{\partial x}, \end{aligned} \quad (1)$$

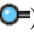
where ψ denotes the streamfunction. (Incompressibility enables us to give an easier formulation, but the results continue to hold for weakly compressible flows.) We are interested in transport of fluid particles in the presence of a *kinematic eddy*, which we define as a moving set of closed streamlines bounded by a time-dependent, singular streamline Φ_t that contains a saddle-type stagnation point $p(t) = (x(t), y(t))$ (see Fig. 1 ). Such a stagnation point will always satisfy

$$\nabla \psi|_{p(t), t} = 0, \quad \det[D^2 \psi|_{p(t), t}] < 0,$$

where $D^2 \psi$ denotes the Hessian matrix of second partial derivatives of ψ . The first condition above simply expresses the fact that $p(t)$ is a stagnation point, while the second condition ensures that $p(t)$ is a saddle point in the contour plot of $\psi(x, y, t)$. This definition of an “eddy” solely in terms of the streamfunction field and not the vorticity may be nonstandard, but it suits our purposes here where the Lagrangian dynamics is a function only of the Eulerian velocity.

Kinematic eddies typically exist for some finite time, say for $t \in [t^-, t^+]$. The $t = t_0$ slices of the two-dimensional surface

$$\Phi = \{(x, y, t_0) | (x, y) \in \Phi_{t_0}, t_0 \in [t^-, t^+]\}$$

serve as instantaneous boundaries for the kinematic eddy. (We recall that Φ_t labels the streamline containing the stagnation point at time t .) For this reason we call the set Φ the *kinematic eddy boundary* (see Fig. 2 ).

Inspired by dynamical systems theory, we expect that under certain conditions the hyperbolic nature of the Eulerian stagnation point $p(t)$ induces hyperbolicity in the corresponding Lagrangian particle dynamics. Roughly speaking, this would mean the existence of a fluid particle motion $\Gamma(t) = (\Gamma_x(t), \Gamma_y(t))$, which behaves like a saddle: it attracts a set $W^s(\Gamma)$ of initial conditions exponentially and repels another set $W^u(\Gamma)$ of initial conditions exponentially. These sets would then act as two-dimensional dividing surfaces in the extended phase space (x, y, t) , and could be used to study transport in the fluid, as described below. Such sets, $W^s(\Gamma)$ and $W^u(\Gamma)$, are called *finite-time stable* and *unstable manifolds*, respectively. They differ from the usual stable and unstable manifolds used in earlier mixing theories in that their definition is not based on infinite time information about particles (see Haller and Poje 1998).

Physically speaking, the above correlation between Eulerian observations (i.e., stream function plots) and Lagrangian dynamics can only be expected to occur if the time dependence of the velocity field (1) is not too fast. This requirement will impose bounds on the maximal velocity

$$\mu = \max_{t \in [t^-, t^+]} |\dot{p}(t)| \quad (2)$$

of the stagnation point, as well as on its speed of rotation, which can be characterized by the rate of change of the eigenvalues and eigenvectors of the Jacobian matrix

$$J(t) = \nabla \mathbf{u}(p(t), t).$$

In particular, let $\lambda(t) > 0$ and $-\lambda(t) < 0$ denote the eigenvalues of $J(t)$, and let us define the quantities

$$\begin{aligned} \lambda_{\max} &= \max_{t \in [t^-, t^+]} \lambda(t), & \lambda_{\min} &= \min_{t \in [t^-, t^+]} \lambda(t), \\ \lambda'_{\max} &\equiv \max_{t \in [t^-, t^+]} |\dot{\lambda}(t)|. \end{aligned} \quad (3)$$

We also introduce the two-by-two matrix $T(t)$ with $\det T(t) = 1$, whose columns are eigenvectors of equal length corresponding to $-\lambda(t)$ and $\lambda(t)$, respectively. We then define the constants

$$t \in [t^-, t^+] \left\| \frac{d}{dt} \right\|$$

where $\beta(t)$ denotes the time-dependent angle enclosed by the eigenvectors.

Physically speaking, the quantities introduced in (2)–(4) measure the rate of streamline deformation near the stagnation point $p(t)$. More concretely, C_T is the maximal angle between the incoming and outgoing directions associated with the saddle-type stagnation point $p(t)$, while C'_T measures the maximal rate at which this angle changes. There is a need for these quantities in our theory since the speed bound μ by itself is not a sufficient measure of the deformation speed of the streamline structure. Indeed, even with $p(t)$ completely fixed in time, the streamline containing $p(t)$ can deform substantially over short timescales.

Hyperbolicity in the Lagrangian dynamics turns out to depend on the nonlinear part of the velocity field as well. To characterize the strength of the nonlinearity near $p(t)$, we consider a small, moving disk of fixed radius C_z centered at the point $p(t)$ that does not contain stagnation points other than $p(t)$. This disk moves together with the stagnation point for times $t \in [t^-, t^+]$, and one can compute numerical bounds on the nonlinear terms of the velocity field \mathbf{v} within the disk. In particular, we will use the quantities

$$C_F = \max_{t \in [t^-, t^+]} \max_{|z| \leq C_z} \frac{1}{2} \|D^2 \mathbf{v}(z + p(t), t)\| \quad (5)$$

with $\|D^2 \mathbf{v}\|$ denoting the Euclidean norm of the three-tensor obtained by differentiating $\nabla \mathbf{v}$, and

$$L_F = \max_i \max_{t \in [t^-, t^+]} \max_{|z| \leq C_z} |\nabla v_i(z + p(t), t) - \nabla v_i(p(t), t)|.$$

Note that both C_F and L_F are scalar constants computed through maximization over the moving disk of radius C_z . They both measure the maximal strength of nonlinear velocity components near $p(t)$. Finally, for convenience, we define the number

$$\bar{C} = \max(C_F C_z, L_F),$$

for use in our later formulas.

As shown in [Haller and Poje \(1998\)](#), if the relations

$$\underbrace{\lambda_{\min}^2 > \lambda'_{\max} + 2C_T \lambda_{\min} (C_T^2 \bar{C} + C'_T)}_{(6)}$$

$$\underbrace{\mu < \left[\frac{\lambda_{\min}^2 - \lambda'_{\max} - C'_T}{2C_T \lambda_{\min}} \right]^2 \times \min \left(\frac{1}{4C_T^2 C_F}, \frac{C_T C_z [1 - C_T^3 C_z C_F]}{\left[\frac{\lambda_{\min}^2 - \lambda'_{\max} - C'_T}{2C_T \lambda_{\min}} - C'_T \right]} \right)}_{(7)}$$

are satisfied, then there exists a hyperbolic fluid particle motion $\Gamma(t)$ with the properties described above. In particular, it admits finite-time stable and unstable manifolds $W^s(\Gamma)$ and $W^u(\Gamma)$, which are exponentially unique in the length of the time interval $[t^-, t^+]$ (see [Fig. 2](#) for geometry). This means that any two stable manifolds to Γ are tangent to each other along Γ . Furthermore, within a tube of radius C_z around Γ in the (x, y, t) space, any two stable manifolds are of order

$$\exp \left(- \int_{t^-}^{t^+} [2\lambda(\tau) - O(\mu, C_z)] \right)$$

close, where the quantity $O(\mu, C_z)$ tends to zero as μ or C_z tends to zero. In other words, for longer Eulerian observations, we obtain exponentially more unique stable and unstable manifolds. This means that $W^s(\Gamma)$ and $W^u(\Gamma)$ can be found numerically with high accuracy.

The finite-time stable and unstable manifolds of Γ separate regions of different dynamical behavior in the flow generated

by (1). We are interested in the case where they separate a bounded set from the rest of the phase space. In that case, inside the bounded set we see swirling motion, while outside the set the motion is translational. We will call such a bounded subset of the (x, y, t) space a *dynamic eddy*. The boundary of the dynamic eddy is defined as the union of pieces of $W^s(\Gamma)$ and $W^u(\Gamma)$ with a “gate” surface through which initial conditions are exchanged. More precisely, let $N(p)$ be a plane that intersects the manifolds $W^s(\Gamma)$ and $W^u(\Gamma)$ transversely as shown in Fig. 2. We define the “gate surface” G as set of points on $N(p)$ that lie between $W^s(\Gamma)$ and $W^u(\Gamma)$, that is, between the two curves γ^u and γ^s . (Note that γ^u and γ^s may intersect, in which case the surface G locally shrinks to a point at the time of intersection.) We consider the surface $S^u \subset W^u(\Gamma)$ bounded by the curves Γ and γ^u , and the surface $S^s \subset W^s(\Gamma)$ bounded by Γ and γ^s . We then define the dynamic eddy as the interior of the cylindrical surface

$$\mathcal{B} = S^u \cup G \cup S^s.$$

It is clearly of interest to determine the flux, $\text{flux}(t)$, of initial conditions through the dynamic eddy boundary \mathcal{B} in order to describe the transport of fluid particles between the eddy and its environment. This flux turns out to be independent of the particular choice of $N(u)$, and obeys the estimate

$$\left| \text{flux}(t) - \frac{A(t) - A(t^-)}{t - t^-} \right| \leq 2 \frac{L(t) + L(t^-)}{t - t^-} \left[\frac{\lambda_{\min} C_B}{\lambda_{\min}^2 - C_A \lambda_{\min} - \lambda'_{\max}} + L_2 \Delta T \right] e^{L_1 \Delta T}, \quad (8)$$

(Click the equation graphic to enlarge/reduce size)

as was shown in Haller and Poje (1998). Here $A(t)$ is the area of the $t = \text{const}$ slice of the kinematic eddy (see Fig. 2); $L(t)$ is the arclength of the boundary of $A(t)$; the constants ΔT , L_1 , and L_2 are defined as

$$\begin{aligned} \Delta T &= \max_{t_0 \in [t^-, t^+]} \max_{|z-p(t_0)| \geq C_z, p \in \phi_{t_0}} \frac{L(t_0)}{|\nabla \psi(z, t_0)|}, \\ L_1 &= 2 \max_i \max_{t \in [t^-, t^+]} \max_{|z-p(t)| \leq C_z} |\nabla v_i(z, t)|, \\ L_2 &= 2 \max_i \max_{t \in [t^-, t^+]} \max_{|z-p(t)| \leq C_z} |\partial_t v_i(z, t)|, \end{aligned}$$

where $z = (x, y)$ and C_A, C_B are small constants depending on the shape of the kinematic eddy boundary. In most oceanographic applications, the right-hand side of Eq. (8) is small, hence the flux can be well approximated by the difference of the kinematic eddy areas at the beginning and at the end of the observation.

3. Numerical model

The double-gyre configuration has become a standard test bed for a number of oceanographic mixing studies (e.g., Figueroa and Olson 1994; Bower and Lozier 1994; Lozier and Riser 1989). Here we use the velocity fields given by a reduced gravity, single layer primitive equation numerical model (see Poje et al. 1996 for details).

Briefly, the shallow water equations,

$$\begin{aligned} \frac{\partial u}{\partial t} + u \frac{\partial u}{\partial x} + v \frac{\partial u}{\partial y} - f_0(1 + \beta y)v &= -g' \frac{\partial h}{\partial x} + F^u + \nu \nabla^2 u \\ \frac{\partial v}{\partial t} + u \frac{\partial v}{\partial x} + v \frac{\partial v}{\partial y} + f_0(1 + \beta y)u &= -g' \frac{\partial h}{\partial y} + F^v + \nu \nabla^2 v \\ \frac{\partial h}{\partial t} + \frac{\partial(uh)}{\partial x} + \frac{\partial(vh)}{\partial y} &= 0, \end{aligned}$$

are solved on a regular grid using second-order finite difference methods. Further, $F^{x,y}$ is the imposed wind stress on the top of the layer and the effects of smaller-scale motions have been subsumed in the Laplacian diffusion terms with “eddy viscosity” coefficient ν ; g' is the reduced gravity, the normal gravitational acceleration weighted by the density difference between the active upper layer and the quiescent lower layer $\Delta\rho/\rho$. No slip boundary conditions are imposed on the velocities at the side walls. The double gyre is set up by imposing a wind stress (F^u, F^v) given by

and $F^{\mathbf{u}} = 0$. The rest of the parameters in the model are chosen as “typical”; see [Table 1](#).

The grid resolution is chosen to adequately resolve spatial features of the flow on scales comparable to the Rossby deformation radius. The total integration time is approximately 10 years. After the initial spinup period, the velocity field was archived twice per simulation day.

The general topology of the double gyre is shown in [Fig. 3](#). The cyclonic subpolar gyre in the north meets the anticyclonic subtropical gyre along the western boundary of the domain. The interaction of the two leads to the formation of a strong, free jet flowing eastward in the center of the domain. This jet is barotropically unstable, resulting in violent meanders of the current about the basin centerline. These meanders intermittently roll up, pinching off cyclonic (anticyclonic) rings or eddies north (south) of the jet. Two such anticyclonic, “warm core” rings are present in the figure. The larger eddies generated by the model have time and length scales comparable to typical Gulf Stream rings; ring radius $l_r \approx 100$ km and life time, from meander pinch off to reentrainment in the western boundary current, on the order of 100–200 days ([Richardson 1983](#)).

Note that the reduced gravity shallow-water model used does not produce a strictly divergence-free velocity field. However, the deviations from exact area preserving flow scale with the size of the ageostrophic component of the velocity field, which is $O(\text{Ro})$. For the flows considered here, the Rossby number, $\text{Ro} = U/Lf$, is small, and the results of [section 2](#) are carried over directly. In each of the following calculations, the difference between the magnitude of the positive and negative eigenvalues of the stagnation point was found to be less than 1%.

4. Ring detachment

a. Eulerian field

[Figures 4a–d](#) show contours of the transport streamfunction in a 1500 km by 1500 km subset of the complete domain at days 95, 110, 140, and 155, respectively; day 0 is chosen at some convenient time during the fifth year of the simulation, well after the initial spinup phase. The subdomain was chosen to isolate the energetic central jet region where eddy shedding takes place.

The stream is loosely defined as locations where the instantaneous depth lies in the range $450 \text{ m} \leq h \leq 550 \text{ m}$. Shallow fluid on the northern side of the jet centerline is contoured dark ($450 \text{ m} \leq h \leq 500 \text{ m}$) while deeper fluid ($450 \text{ m} \leq h \leq 500 \text{ m}$) to the south is contoured in lighter shades. Only those regions where the depth lies between 450 and 550 m are contoured. For ease of notation and to allow qualitative comparisons with Gulf Stream observations, shallow fluid north of the jet is considered cold, while deep, southern fluid is warm.

The times series of depth contours shows the birth of a cold core ring from an extreme southwestern meander of the jet near $(x, y) \sim (800 \text{ km}, 800 \text{ km})$. Also evident in the plots is the formation of a warm core ring from an extreme northerly meander immediately downstream of the first ring. The entire series from the birth of a frozen time saddle point at the northern edge of the meander loop ([Fig. 4a](#)) until the completion of pinch off ([Fig. 4d](#)) takes approximately 60 days of simulation time.

b. Existence of the hyperbolic trajectory

The Eulerian time slices provide the data necessary for determining the existence of a controlling hyperbolic trajectory in the Lagrangian particle dynamics. The location and the eigenvalues of the stagnation point were computed at two-day intervals over a 100-day time period. The results are shown in [Fig. 5](#). The fixed point is born, the eigenvalues of the linearization grow in time to a maximum at approximately $t = 70$ days and then decay as the newly formed ring moves westward away from the jet core. Note that a stagnation point exists in the fixed time slices whenever there is an identifiable ring structure. Kinematically, some location must exist between the jet and the center of the ring where the velocity vector is zero. While this hyperbolic region exists in individual Eulerian snapshots, it is not expected to heavily impact on the Lagrangian dynamics if the conditions of [section 2](#) are not met.

The estimates in [Eq. \(6\)](#) for the minimum allowable eigenvector and maximum allowable speed of the fixed point $p(t)$ depend upon two derivative measures of velocity field in local neighborhood of fixed point. The 10-km grid resolution of the numerical scheme leads to a choice of $C_z = 40$ km, thus maximization over $|z| < C_z$ corresponds to maximization of the numerical fields on the 8×8 matrix of values centered on the grid box containing $p(t)$. In this way, L_f and C_f are computed to be

$$L_f \cong 0.015 \text{ day}^{-1}, \quad C_f \cong 0.002 \frac{1}{\text{day km}}.$$

The eigenvectors associated with $p(t)$ were computed at 5-day intervals and normalized so that the matrix of eigenvectors

has a determinant of one. The maximum values of the matrix norm of T and its time derivative are given by

$$C_T = 1.06, \quad C'_T = 0.0015 \text{ day}^{-1}.$$

Figure 6 shows the time series of the square of the eigenvalues of $p(t)$ along with a numerical estimate of the right-hand side of the of Eq. (6). The plot shows that $\lambda^2(t)$ is greater than the quantity $\lambda'_{\max} + 2C_T\lambda_{\min}(C_T^2\bar{C} + C'_T)$ for almost all times in the interval $10 < t < 100$ days. For the period of time $35 < t < 100$ days, after the initial formation of the ring and during the slow west-southwestward drift of the structure, the inequality is well satisfied. In other words, the timescale of the hyperbolicity is fast compared with the timescale of changes in the hyperbolicity. The second estimate concerning the speed of the fixed point, $\mu = \max[\dot{P}(t)]$ is also satisfied, but on a slightly restricted time frame. Using λ_{\min} and λ'_{\max} for $40 < t < 80$ days, Eq. (7) gives $\mu < 6 \text{ km day}^{-1}$. From Fig. 5, the fixed point moves westward at speeds less than 3.5 km day^{-1} during this time period.

c. Lagrangian dynamics

In two-dimensional flow the position of a Lagrangian particles is given by

$$\dot{\mathbf{x}} = \mathbf{u}(x, y, t) \quad \dot{\mathbf{y}} = \mathbf{v}(x, y, t), \quad (9)$$

where $u(x, y, t)$ and $\mathbf{v}(x, y, t)$ are, respectively, the Eulerian east-west and north-south velocity fields given by solutions of the shallow water equations. As numerical solutions, the Eulerian fields are known only at discrete spatial and temporal points, and thus must be interpolated in order to solve Eq. (9). The numerical techniques for doing this are described fully in Miller et al. 1997.

Three representative solutions to Eq. (9) are shown in Fig. 7. The particles were initialized in the stream on day 10 at $x = 450 \text{ km}$ and $y = 940, 970, \text{ and } 1000 \text{ km}$, respectively. Although separated by relatively small cross-stream distances, the three trajectories are markedly different. The northernmost particle follows the stream before slowing considerably in the region near the detaching ring and eventually meandering to the north. After approximately 24 days the particle released at $y = 970 \text{ km}$ is fully entrained in the ring, executing several revolutions in the 100 days plotted. The southernmost particle passes south of the detaching cold core ring, slowing near the hyperbolic trajectory.

d. Lagrangian invariant manifolds

In order to locate the sets of initial conditions that are eventually entrained into the detaching ring and to examine the geometry of the transient mixing event, the finite-time manifolds associated with the hyperbolic point are constructed numerically. This is accomplished by tracking the location of small line segments initially aligned with the directions of the stable (compressing) and unstable (stretching) eigenvectors of the fixed time, Eulerian saddle point.

The numerical approximation to W^u , the unstable manifold, is found by initializing a short line segment on the unstable eigendirection at time $t_i = 10$ days. This segment is then integrated forward under the flow (see Figs. 8 and 9). Due to the near exponential stretching in the vicinity of the hyperbolic point, the short initial segment rapidly grows. Compression in the transverse, stable direction ensures that small errors in the alignment of the initial segment decay rapidly.

Calculation of W^s , the stable manifold, is done in a similar manner. Starting at time $t_i = 70$ days, a line segment is initialized along the stable eigendirection of the Eulerian stagnation point. This set is then evolved backward in time under the flow to produce the stable manifold.

Figures 8 and 9 show the numerically generated manifolds at times $t = 10, 20, 35, \text{ and } 45$ days: the unstable manifold increasing in length as time progresses forward and the stable set growing in backward time.

The manifolds are invariant under the flow; in other words, particles initially in these sets remain in the sets. In the extended phase space (x, y, t) , the manifolds sweep out two-dimensional surfaces dividing the phase space volume into distinct regions (see Fig. 2). Due to the uniqueness of solutions, fluid particles cannot cross the extended manifolds; hence they act as barriers to particle motion. In particular, the elongated mixing channel enclosed between the two branches of the stable manifold separates the set of initial conditions that ultimately find their way into the eddy from those that do not.

Due to the fast particle speeds in the stream, the hyperbolic nature of the detaching eddy has a significant nonlocal effect. The extreme length of the mixing channel implies that the eddy entrains a significant amount of fluid from far downstream in the jet itself, not simply from the surrounding water mass. In Fig. 10 the computed stable manifold at day 10 is superimposed on the three individual particle trajectories computed in Fig. 7. Only the fluid particle initially launched within the mixing channel is entrained in the recirculating eddy. The thinness of the channel explains the sensitive dependence of the particle trajectories on initial cross-stream position.

The dynamic Lagrangian boundary of the ring is given by the intersection of $W^s(\Gamma)$, $W^u(\Gamma)$ and a gate surface G , as shown schematically in [Fig. 2](#). While Eulerian observations of the size of the kinematic eddy lead to estimates of scalar flux, the Lagrangian evolution of the dynamic eddy boundary and the gate surface indicates exactly which particles participate in the transport process. We define two gate surfaces, given by the line $y = 850$ km at different times: G_2 is this line at $t = 22$ days and G_1 is the line at $t = 35$ days. With these in place, there are four intersection points: (q_1, q_2, \dots) . The two regions, R_I and R_{II} , are defined as the area enclosed by the following boundaries:

$$\begin{aligned}\partial R_I &= G_1 \cup W^s(q_1, q_4) \cup G_2 \cup W^u(q_3, q_2) \\ \partial R_{II} &= G_2 \cup W^s(q_4, \Gamma) \cup W^u(\Gamma, q_3),\end{aligned}$$

where Γ is the hyperbolic intersection point of W^s and W^u ; the notation $W^s(q_1, q_4)$ denotes the segment of the stable manifold between the intersection points q_1, q_4 . The geometry for this example is shown in [Fig. 11](#).

Neglecting changes in layer depth, the area flux of fluid particles into the emerging ring can be obtained directly by calculating changes in the area of the dynamic eddy boundary as defined above. Sample flux calculations are shown in [Fig. 12](#) along with estimates of the particle flux obtained by direct observation of the Eulerian, “kinematic” eddy area. Here this area is defined by the *homoclinic loop*, the largest closed streamline in a particular, frozen time slice. In this example, the fluxes computed from differences in Eulerian areas and the actual, dynamic particle flux estimated from the manifold geometry compare well with an average flux of 3 Sv. The Lagrangian analysis indicates a trend toward increasing particle flux into the ring during its westward propagation.

In order to show which initial conditions are entrained by the detaching ring over a longer time period, we redefine the gate surfaces. At time $t_0 = 10$ days, G_2 is the line that joins the two legs of the mixing channel at $x = 470$ km; G_1 joins the stable and unstable manifolds at $x = 910$ km. The domain is thus split into two closed regions R_I and R_{II} ; the evolution of these two regions is shown for a 50-day time period in [Fig. 13](#).

During this interval the emerging ring has doubled in size ($\text{Area}_{R_I} \approx \text{Area}_{R_{II}}$). As shown, the outer fluid in the eddy at time t_f originates in an elongated region extending several hundred kilometers upstream from the detachment point at time t_0 . Note that the majority of the marked fluid particles were initialized in the subpolar gyre, that is, north of the 500-m depth contour shown in bold on [Fig. 13](#). Thus, during the 50-day time period considered, these initial conditions were transported from the subpolar to the subtropical gyre by the detaching ring. Also, the presence of a hyperbolic trajectory leads to extremely high rates of stretching for fluid elements entering the ring. During the time period considered, the length of the interfacial line marking the boundary of regions I and II has stretched to almost 20 times its initial length. The thin mixing channel ensures that the trajectories of entrained particles pass close to the hyperbolic trajectory, and thus area elements are highly stretched in one direction while being compressed in the other.

In general, the slow evolution of the structure leads to an “adiabatic” like transport geometry (see, e.g., [Kaper and Kovačić 1994](#)). The mixing regions are long and thin, the length given by the ratio of Eulerian to Lagrangian timescales, and the thickness given by the inverse of that ratio.

f. Mixing

To demonstrate the general organizing influence of the finite time manifolds on the Lagrangian dynamics, we examine the evolution of two distinct sets of initial conditions in the jet region.

[Figure 14](#) shows the Lagrangian evolution of an initially circular mass of fluid straddling the instantaneous location of the jet. The set of points evolves in a complicated manner: different elements recirculating north and south of the jet, traveling eastward or becoming trapped in the detaching rings. The small area of fluid initially within the mixing channel will eventually become part of the recirculating eddy. All other elements of the initial area will eventually lie outside the ring. The unstable manifold (W^u) acts as a barrier to particle motion, producing extreme amounts of stretching in nearby fluid.

[Figure 15](#) shows a similarly sized region of fluid, initialized to lie entirely within the mixing channel given by the computed stable manifold. Each fluid particle in this elongated region is eventually mapped into the cold core ring. In this case, the Lagrangian dynamics are quite tame since every element of the initial blob must, due to the presence of the stable manifold channel, simply flow into the recirculating region.

5. Ring-stream interaction

Typically, eddies detached from the stream will propagate westward, eventually becoming reentrained in the western boundary current. Intermittently, such a detached ring will interact with the meandering jet. In the process, fluid is

exchanged in both directions between the eddy and the jet. The Eulerian time series of an ring–jet interaction event is shown in [Fig. 16](#). Here a warm core eddy is propagating westward to the north of the jet. The velocity induced by the ring acts to lift the jet northward. In [Fig. 16a](#), the two structures collide, giving rise to a homoclinic loop in the Eulerian streamfunction plots. The eddy and jet interact for a considerable period of time until eventually the eddy is completely absorbed in the stream. Here we study the exchange geometry during the initial encounter.

Analysis of the strength and location of the saddle-type stagnation point in the Eulerian data indicate that the estimates of [section 2](#) are more easily satisfied than they were for the detaching ring flow. The location $p(t)$ of the stagnation point is almost fixed in time near $x = 650$, $y = 1050$. The strength of the hyperbolicity varied between $\lambda = 0.3 \text{ day}^{-1}$ and $\lambda = 0.5 \text{ day}^{-1}$ during the time analyzed.

a. Lagrangian manifolds

As in the eddy shedding case above, we calculate numerical approximations to the local Lagrangian manifolds using the Eulerian snapshots as a guide. The unstable manifold calculation was initialized at reference time $t_0 = 10$ days; the stable manifold 100 days later.

The computed manifolds are shown in [Fig. 17](#) with enlargements shown in [Figs. 18a–c](#). In this case, where fluid is mixed both into and out of the ring, we find an additional intersection point of W^s and W^u . At time $t = 50$ days, both branches of W^s intersect W^u near the hyperbolic point, p (see [Fig. 18](#) for details). The ring area enclosed by the loop of W^s in [Fig. 18a](#) defines the initial conditions that will remain within the eddy. The thin region lying inside W^u and outside of W^s (region II in the figure) marks the set of initial conditions that will be mixed from the eddy into the jet.

As time progresses, the second intersection point (p_1 in [Fig. 18b](#)) travels clockwise along the eddy exterior. At time $t = 60$ days, there are three distinct regions within the eddy as shown in [Fig. 18b](#). The central core (region I) does not take part in the mixing. Region III, defined by the area inside the two branches of W^s , consists of fluid being mixed into the eddy, while region II, inside the two branches of W^u , consists of fluid being returned to the jet by the eddy.

Finally, at time $t = 70$ days, the secondary intersection point has moved farther along the outside of the ring. Again particles are exchanged from the jet in region III and to the jet in region II. Note that while the kinematic picture given by Eulerian snapshots of the flow in the case of eddy–jet interaction is very similar to that for the detaching ring scenario, the particle dynamics and mixing are quite different, and this difference is evident in the manifold geometry.

b. Mixing

The mixing of fluid from the eddy to the jet is shown in [Fig. 19](#). A set of initial conditions, contained completely within the Lagrangian eddy defined in [Fig. 17a](#), is marked in red and evolved forward under the flow. First a thin ribbon of fluid is shed from the exterior of the eddy, as indicated by the manifold geometry in [Fig. 17](#). Eventually a larger mass of fluid is expelled, this originating in the lobe area of region II (see first panel of [Fig. 17](#)). This eddy to jet mixing channel is eventually replaced with jet to eddy exchange as evidenced by the lack of any further exchange between the circular mass within the eddy and the contorted area now in the jet.

6. Discussion

In this paper we have shown how recent mathematical results allow the application of geometric techniques to the study of Lagrangian particle dynamics in oceanic flows with general time dependence. If one can isolate a saddle-type stagnation point in the Eulerian velocity data and the structure of this point deforms slowly relative to the advective timescale of the particles, then a corresponding hyperbolic trajectory exists in the Lagrangian dynamics. The finite-time stable and unstable manifolds associated with this trajectory act as controlling surfaces for Lagrangian mixing and transport in the flow. The estimates given in [section 2](#) provide an a priori means of determining, from Eulerian velocity data, whether or not such a controlling hyperbolic trajectory exists.

The dynamical systems theory of aperiodic mixing guarantees that the finite-time invariant manifolds described above are numerically robust, that is, unique up to exponentially small errors. Using these sets as templates, one can obtain a complete understanding of the dynamical features of a two-dimensional flow based on the integration of one-dimensional segments of initial conditions. This requires substantially less computational power than integrating the velocity field on a two-dimensional grid.

For the dynamically consistent, double gyre velocity field considered here, the majority of mixing events involving mesoscale coherent structures such as rings are amenable to analysis in this way. The resulting geometric picture of the Lagrangian flow field has several notable features.

In the case of ring formation the manifold geometries, and hence the dynamics, are dominated by the existence of a *mixing channel*, formed by the two legs of the stable manifold, through which particles are entrained into the ring. The invariance of the manifold implies that, at any time, only those particles contained within this channel will be entrained into

the detaching ring. As seen in [Figs. 8](#) and [9](#), the channel consists of a teardrop-shaped area enclosed by the detaching ring and a highly elongated region that exists initially on the northern side of the jet core and extends far upstream, nearly into the western boundary current. The detaching ring thus entrains not only nearby fluid but first northern and then southern jet water from remote distances. This “stripping” of jet fluid by the eddy or ring is very similar to that seen in eddy–jet interactions studied by both [Stern and Flierl \(1987\)](#) and [Bell and Pratt \(1992\)](#). Here however, the ring (vortex) is born out of the jet and is therefore capable of stripping fluid from both the near and far side of the stream. The enhanced mixing of a meandering jet in the presence of an eddy ([Dutkiewicz and Paldor 1994](#)) can be directly attributed to the presence of highly elongated Lagrangian structures that map, in the time periodic case, fluid into and out of the eddy ([Haller and Poje 1997](#)).

The existence of a Lagrangian invariant surface that extends far upstream of the detaching ring implies that there is no direct intergyre particle exchange in this upstream region during the time period considered. The manifold is invariant under the flow, and thus particle trajectories may not cross it. As in both the two-layer dynamic simulation of [Bower and Lozier \(1994\)](#) and the kinematic model of [Yang \(1996a,b\)](#), particle transport across the jet core is confined to the eastern part of the basin where potential vorticity gradients have weakened. In the western half, where the jet and associated potential vorticity gradients are strongest, the manifold geometry points to a very sensitive dependence of eventual particle dynamics on initial conditions. The mixing channel is extremely narrow in this region, and, as shown by the particle trajectories in [Fig. 10](#), the jet region is filamented by particles that are eventually mixed by the detaching ring. We note that the presence of a warm core ring, detaching upstream of the cold core ring studied, further filaments the jet core due to the action of its own Lagrangian mixing channel.

A slightly more complex geometry exists during the interaction of a ring with the meandering jet. In this case, the computed finite-time stable and unstable manifolds intersect at two distinct points, indicating transport of fluid particles in both directions between the jet and the ring. The precise nature of the transport between the two regions is readily analyzed by following the secondary intersection point of $W^u(\Gamma)$ and $W^s(\Gamma)$. Initially, the bulk of the exchange is from the ring into the jet. As the ring begins to propagate westward, it entrains fluid from the jet. The mixing, in either case, is confined to thin filaments along the exterior of the ring and the core is unaffected.

In general, it appears that a number of hyperbolic points exist in any eddy resolving flow such as the one examined in this paper, and each hyperbolic point satisfying the conditions of slow deformation and motion will have associated finite-time manifolds. The dynamics of Lagrangian particles are, at least for intermediate timescales, determined completely by the geometry and interaction of these various manifolds. An important open question is how these individual geometric structures influence the overall statistics of the particle motion. The anisotropy of the computed mixing channels points to anisotropy in the dispersion statistics while the near exponential stretching associated with the manifolds may be responsible for observed anomalous dispersion rates.

Acknowledgments

We would like to thank Chris Jones, Denny Kirwan for helpful discussions, and Pat Miller for introducing us to his results. This research was supported by ONR Grant N00014-93-I-0691, and partially supported by NSF Grant DMS-98-00922 and an Alfred P. Sloan Fellowship.

REFERENCES

- Bell, G. I., and L. J. Pratt, 1992: The interaction of an eddy with an unstable jet. *J. Phys. Oceanogr.*, **22**, 1229–1244. [Find this article online](#)
- Bower, A. S., 1991: A simple kinematic model for mixing fluid particles across a meandering jet. *J. Phys. Oceanogr.*, **21**, 173–180. [Find this article online](#)
- , and H. T. Rossby, 1989: Evidence of cross-frontal exchange processes in the Gulf Stream based isopycnal RAFOS float data. *J. Phys. Oceanogr.*, **19**, 1177–1190. [Find this article online](#)
- , and M. S. Lozier, 1994: A closer look at particle exchange in the Gulf Stream. *J. Phys. Oceanogr.*, **24**, 1399–1418. [Find this article online](#)
- Dutkiewicz, S., and N. Paldor, 1994: On the mixing enhancement in a meandering jet due to the interaction with an eddy. *J. Phys. Oceanogr.*, **24**, 2418–2423. [Find this article online](#)
- Figueroa, H. A., and D. B. Olsen, 1994: Eddy resolution versus eddy diffusion in a double gyre GCM. Part I: The Lagrangian and Eulerian description. *J. Phys. Oceanogr.*, **24**, 371–386. [Find this article online](#)
- Haller, G., and A. C. Poje, 1997: Eddy growth and mixing in mesoscale oceanographic flows. *Non-linear Proc. Geophys.*, **4**, 223–235.
- , and —, 1998: Finite time transport in aperiodic flows. *Physica D*, **119**, 352–380.
- Kaper, T. J., and G. Kovacic, 1994: A geometric criterion for adiabatic chaos. *J. Math. Phys.*, **35**, 1202–1218.

Lozier, M. S., and S. C. Riser, 1989: Potential vorticity dynamics in a quasi-geostrophic ocean. *J. Phys. Oceanogr.*, **19**, 1373–1396.. [Find this article online](#)

—, L. J. Pratt, A. M. Rogerson, and P. D. Miller, 1997: Exchange geometry revealed by float trajectories in the Gulf Stream. *J. Phys. Oceanogr.*, **27**, 2327–2341.. [Find this article online](#)

Mackay, R. S., J. D. Meiss, and I. C. Percival, 1984: Transport in Hamiltonian systems. *Physica D*, **13**, 55–81..

Melander, M. V., J. C. McWilliams, and N. J. Zabusky, 1987: Axisymmetrization and vorticity-gradient intensification of an isolated two-dimensional vortex through filamentation. *J. Fluid Mech.*, **178**, 137–159..

Miller, P. D., C. K. R. T. Jones, A. M. Rogerson, and L. J. Pratt, 1997: Quantifying transport in numerically generated velocity fields. *Physica D*, **110** 1–18..

Owens, W. B., 1984: A synoptic and statistical description of the Gulf Stream and subtropical gyre using SOFAR floats. *J. Phys. Oceanogr.*, **14**, 104–113.. [Find this article online](#)

Poje, A. C., D. A. Jones, and L. G. Margolin, 1996: Enslaved finite difference approximations for quasi-geostrophic shallow flows. *Physica D*, **98**, 559–573..

Polvani, L. M., G. R. Flierl, and N. J. Zabusky, 1989: Filamentation of unstable vortex structures via separatrix crossing: A quantitative estimate of onset time. *Phys. Fluids A*, **2**, 181–184..

Richardson, P. L., 1983: Gulf Stream rings. *Eddies in Marine Science*, A. R. Richardson, Ed., Springer-Verlag, 19–45..

Ridderinkhof, H., and J. W. Loder, 1994: Lagrangian characterization of circulation over submarine banks with application to the Gulf of Maine. *J. Phys. Oceanogr.*, **24**, 1184–1200.. [Find this article online](#)

Rom-Kedar, V., A. Leonard, and S. Wiggins, 1990: An analytical study of transport, mixing, and chaos in an unsteady vortical flow. *J. Fluid Mech.*, **214**, 347–394..

Samelson, R. M., 1991: Fluid exchange across a meandering jet. *J. Phys. Oceanogr.*, **21**, 431–440.. [Find this article online](#)

Song, T., H. T. Rossby, and E. Carter, 1995: Lagrangian studies of fluid exchange between the Gulf Stream and surrounding waters. *J. Phys. Oceanogr.*, **25**, 46–63.. [Find this article online](#)

Stern, M. E., and G. R. Flierl, 1987: On the interaction of a vortex with a shear flow. *J. Geophys. Res.*, **92**, 10 733–10 744..

Wiggins, S., 1992: *Chaotic Transport in Dynamical Systems*. Springer-Verlag, 301 pp..

Yang, H., 1996a: The subtropical/subpolar gyre exchange in the presence of annually migrating wind and a meandering jet: Water mass exchange. *J. Phys. Oceanogr.*, **26**, 115–130.. [Find this article online](#)

—, 1996b: Lagrangian modeling of potential vorticity homogenization and the associated front in the Gulf Stream. *J. Phys. Oceanogr.*, **26**, 2480–2496.. [Find this article online](#)

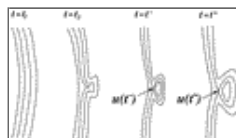
Tables

Table 1. Parameter values for the numerical model.

Coriolis parameter ($f = f_0 + \beta y$)	$f_0 = 6.3 \times 10^{-2} \text{ s}^{-1}$	$\beta = 0.66 (\text{C} \times 10^{-11} \text{ m}^{-1} \text{ s}^{-2})$
Initial state	$u_0 = 0.1 \text{ m s}^{-1}$	$v_0 = 0.1 \text{ m s}^{-1}$
Viscosity parameter	$\nu = 175 \text{ m}^2 \text{ s}^{-1}$	$\kappa = 0.02 \text{ m}^2 \text{ s}^{-1}$
Effective gravity	$g' = 0.02 \text{ m s}^{-2}$	$H_0 = 500 \text{ m}$
Initial separation depth		
Domain	East-west $L_x = 2000 \text{ km}$	North-south $L_y = 2000 \text{ km}$
Grid resolution:	$\Delta x = 10 \text{ km}$	$\Delta y = 10 \text{ km}$
Boundary deformation radius	$R_D = (g'H_0/f_0^2)^{1/2}$	$R_D = 36\text{--}23 \text{ km}$

[Click on thumbnail for full-sized image.](#)

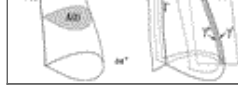
Figures



[Click on thumbnail for full-sized image.](#)

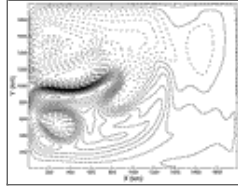
Fig. 1. The formation of a kinematic eddy.





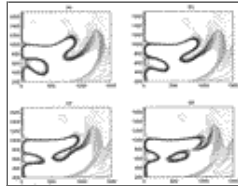
[Click on thumbnail for full-sized image.](#)

Fig. 2. The geometry of a finite-time mixing event.



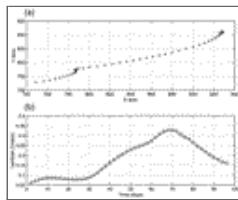
[Click on thumbnail for full-sized image.](#)

Fig. 3. Topology of the double-gyre circulation. Contours of the instantaneous layer depth $h(x, y, t)$ sometime during year 5 of the simulation. Depths less than 500 m are shown dashed.



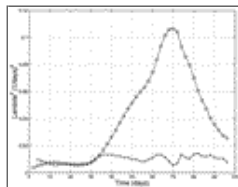
[Click on thumbnail for full-sized image.](#)

Fig. 4. Layer depths in the subdomain at four different times during the formation of a cold core ring. Contour information in the text. (a) $t = 10$ days, (b) $t = 30$ days, (c) $t = 50$ days, and (d) $t = 70$ days.



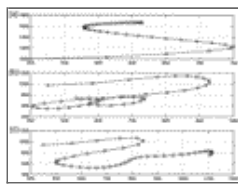
[Click on thumbnail for full-sized image.](#)

Fig. 5. The location of the frozen time stagnation point, $\mathbf{p}(t)$, and the the strength of the hyperbolicity, $\lambda(t)$, for the detaching cold core ring.



[Click on thumbnail for full-sized image.](#)

Fig. 6. Inverse timescales of the hyperbolicity and the rate of change of hyperbolicity for the cold core eddy during detachment. $\lambda^2(t)$: open circles; $\dot{\lambda}(t)$: plus signs.



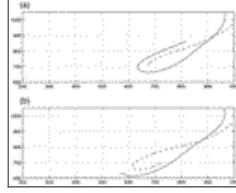
[Click on thumbnail for full-sized image.](#)

Fig. 7. Trajectories of three different Lagrangian particles released in the stream on day 10. Circles mark positions at two day intervals.



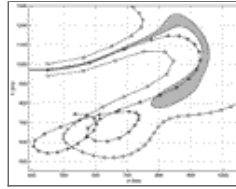
[Click on thumbnail for full-sized image.](#)

Fig. 8. Invariant manifolds of the cold core ring at $t = 10$ days (top) and $t = 20$ days (bottom). Stable manifold W^s solid; unstable manifold W^u dashed.



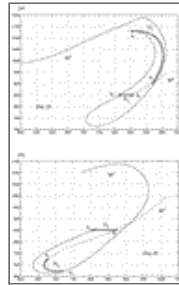
[Click on thumbnail for full-sized image.](#)

Fig. 9. Invariant manifolds of the cold core ring at $t = 35$ days (top) and $t = 48$ days (bottom). Stable manifold W^s solid; unstable manifold W^u dashed.



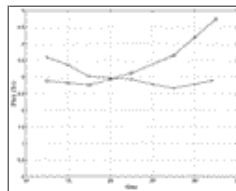
[Click on thumbnail for full-sized image.](#)

Fig. 10. Local stable manifold and mixing channel (shaded) superimposed on three particle trajectories. The stable manifold corresponds to day 10, the launch date for the particles.



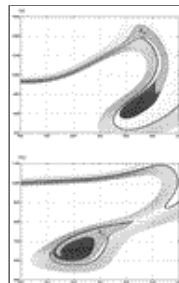
[Click on thumbnail for full-sized image.](#)

Fig. 11. Geometry of the dynamic eddy boundary used in flux calculation.



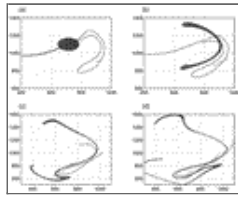
[Click on thumbnail for full-sized image.](#)

Fig. 12. Particle flux calculated from the dynamic Lagrangian and kinematic, Eulerian eddy areas. Eulerian calculation marked with +; Lagrangian with \odot . Flux given in Sverdrup units ($1 \text{ Sv} = 10^6 \text{ m}^3 \text{ s}^{-1}$).



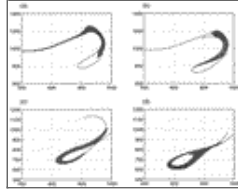
[Click on thumbnail for full-sized image.](#)

Fig. 13. Mixing regions and depth contours for the detaching ring at days 10 and 60. The location of the 500-m depth line is shown in bold.



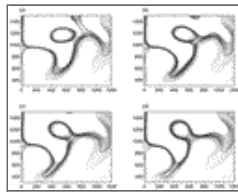
[Click on thumbnail for full-sized image.](#)

Fig. 14. Mixing of a circular set of initial conditions. Marked particles are shown shaded, lines indicate computed manifolds: (a) $t = 10$ days, (b) $t = 20$ days, (c) $t = 35$ days, and (d) $t = 50$ days.



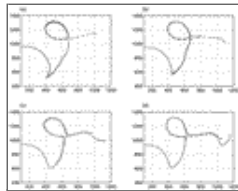
[Click on thumbnail for full-sized image.](#)

Fig. 15. Evolution of initial conditions lying within the mixing channel. Marked particles are shaded, lines indicate computed manifolds. (a) $t = 10$ days, (b) $t = 20$ days, (c) $t = 35$ days, and (d) $t = 50$ days.



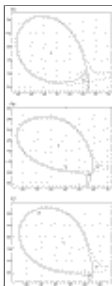
[Click on thumbnail for full-sized image.](#)

Fig. 16. Layer depths at four different times during the interaction between a warm core ring and the jet. Depth field contours explained in text. (a) $t = 40$ days, (b) $t = 50$ days, (c) $t = 60$ days, and (d) $t = 80$ days.



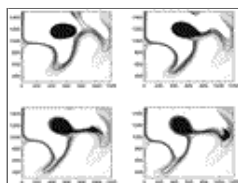
[Click on thumbnail for full-sized image.](#)

Fig. 17. Local Lagrangian manifolds during the eddy-jet interaction. W^s solid; W^u dashed. (a) $t = 40$ days, (b) $t = 50$ days, (c) $t = 60$ days, and (d) $t = 80$ days.



[Click on thumbnail for full-sized image.](#)

Fig. 18. (a) Enlargement of the local manifolds near the hyperbolic point at time (a) $t = 50$, (b) $t = 60$, and (c) $t = 70$ days. The primary hyperbolic point is at p , secondary intersection at $p1$.



[Click on thumbnail for full-sized image.](#)

Fig. 19. Mixing from eddy to jet. Marked particles shown shaded; depth field contoured as in text for (a) $t = 40$ days, (b) $t = 50$

days, (c) $t = 70$ days, and (d) $t = 80$ days.

Corresponding author address: Andrew Poje, Division of Applied Mathematics, Box F, Brown University, Providence, RI 02906.

E-mail: poje@cfm.brown.edu

top ▲



© 2008 American Meteorological Society [Privacy Policy and Disclaimer](#)
Headquarters: 45 Beacon Street Boston, MA 02108-3693
DC Office: 1120 G Street, NW, Suite 800 Washington DC, 20005-3826
amsinfo@ametsoc.org Phone: 617-227-2425 Fax: 617-742-8718
[Allen Press, Inc.](#) assists in the online publication of *AMS* journals.